nature communications

Article

https://doi.org/10.1038/s41467-025-60388-y

Lunar dichotomy in surface water storage of impact glass beads

Received: 21 December 2024

Accepted: 22 May 2025

Published online: 29 May 2025

Check for updates

Huicun He[1], Sen Hu[1,2] ✉, Liang Gao[1,2], Ruiying Li[1], Jialong Hao[1], Ross N. Mitchell[2,3], Kai Lu[3], Yubing Gao[1,2], Linxi Li[1,2], Mengfan Qiu[1,2], Zhan Zhou[1,2], Wei Yang[1], Shuhui Cai[3], Yi Chen[3], Lihui Jia[3], Qiu-Li Li[3], Hejiu Hui[4], Yangting Lin[1], Xian-Hua Li[3] & Fu-Yuan Wu[3]

Water is the one of most precious resources for planetary utilisation. Lunar nearside impact glass beads (IGBs) have been demonstrated to contain abundant solar wind-derived water (SW-H_2O); however, little is known about its farside counterpart. Here, we report the water abundances and hydrogen isotope compositions and their distribution in farside IGBs collected by the Chang'e-6 mission to investigate the role of IGBs in the lunar surface water cycle. Farside IGBs are found to have water abundances of ~10–1,070 μg.g^{-1} with hydrogen isotopes (δD) ranging from −988‰ to >2000‰ and display typical SW-H_2O hydration profiles. The SW-H_2O hydration depths in farside IGBs are strikingly shallower than in nearside IGBs. Moreover, the hydration profiles are only found in mare IGBs, with none observed in non-mare IGBs, indicating that SW-H_2O hydration in IGBs is likely composition dependent. These findings indicate that SW-H_2O storage of IGBs exhibits a dichotomy distribution in lunar soils.

Water is critical for life, plays a fundamental role in the evolution of planets[1], moons[2,3], and asteroids[4], and is one of the most precious resources for planetary utilisation[5,6]. One of the biggest advances in lunar and planetary sciences in the past two decades was the discovery of water on the Moon[7–18], which has inspired the potential for in situ water utilisation in future lunar base construction (Artemis) and lunar research stations (CE7 and post-CE missions)[19]. Planetary water, generally defined, includes H/H_2, OH, and H_2O in various forms[9,10,20]. Lacking an atmosphere, the Moon on its surface is a typical airless celestial body, characterised by a high vacuum (10^{-12}–10^{-10} torr; ref. 21.), strong irradiation[22], large diurnal temperature variations (about −150 to +150 °C, ref. 23.), and numerous impact craters[24]. Therefore, the existence of water on the Moon under such harsh environmental conditions is surprising and can inform our understanding of the presence of water on other airless bodies in the Solar System[25,26].

Water on the Moon has been detected to have concentrations ranging from ~10–1000 μg.g^{-1} (ref. 7), which generally increase from the equator to the polar regions and exhibits temporal variations due to fluctuating surface temperature as inferred from the near-infrared spectroscopy observations of the Chandrayaan-1 probe[27–29]. Larger amounts of water (up to 56 ± 29 mg.g^{-1}), probably in the form of water ice, were detected in the permanently shadowed region within Cabeus crater located close to the South Pole as predicted by impact experiments[8] and later confirmed by neutron spectroscopy observations[15]. Molecular water was also detected on the lunar mid-latitude surface[9,17]. The spatiotemporal variations of lunar surface water[27–29] and the detection of exospheric water release to space[30] suggest that surface water on the Moon displays dynamic retention, release, and replenishment processes, inspiring hypothesis of a lunar surface water cycle[30,31].

[1]Key Laboratory of the Earth and Planetary Physics, Chinese Academy of Sciences, Beijing, China. [2]College of Earth and Planetary Sciences, University of Chinese Academy of Sciences, Beijing, China. [3]State Key Laboratory of Lithospheric and Environmental Coevolution, Institute of Geology and Geophysics, Chinese Academy of Sciences, Beijing, China. [4]State Key Laboratory for Mineral Deposits Research& Lunar and Planetary Science Institute, School of the Earth Sciences and Engineering, Nanjing University, Nanjing, Jiangsu, China. ✉e-mail: husen@mail.iggcas.ac.cn

A hydrated layer at depth in lunar soils has been proposed on the basis of such a hypothesised lunar surface water cycle[30]. Impact glass beads (IGBs)—a common component in lunar soils produced by asteroid impacts[32]—collected by the Chang'e-5 (CE5) mission from the lunar nearside have been demonstrated to contain abundant solar wind-derived water (SW-H_2O)[16,17]. The CE5 IGBs have SW-H_2O hydration profiles typically up to 40 μm deep, suggesting that IGBs in lunar soils may be one of the most important components sustaining the lunar surface water cycle[16]. It is currently unknown, however, if IGBs in the lunar soils from different geographic locations on the Moon record similar or different SW-H_2O hydration features. Such a geographic and geologic context for IGBs is critical to understanding their potential role in the lunar surface water cycle and deepen our knowledge of the origin, storage, and distribution of water on the Moon and other airless bodies. Thus, newly discovered IGBs in the first lunar soils from the farside of the Moon recently collected by the Chang'e-6 (CE6) mission, located thousands of kilometers away from previous collections, can be used to investigate the homogeneity or heterogeneity of the distribution of surface water on the Moon.

Here, we perform systematic analyses of water abundances, hydrogen isotopes, and chemical compositions of CE6 IGBs to unravel the distribution and mechanism of SW-H_2O storage in lunar farside soils, finding that SW-H_2O storage of IGBs exhibits a dichotomy distribution in the lunar soils.

Results and discussion

Distribution of water in CE6 impact glass beads

Among the 263 hand-picked particles from two scooped lunar soils (CE6C0200YJFM001, ~5 g and CE6C0300YJFM002, ~6 g), a total of 77 grains were identified as impact glass beads (IGBs) (Supplementary Fig. 1 and Data 1). About 36% (28) of the CE6 IGBs exhibiting smooth surfaces without exposed Fe-Ni metals, mineral clasts, and bubbles (Fig. 1 and Supplementary Figs. 1, 2, 3) were selected for in situ ion probe measurements of water abundances and hydrogen isotopic compositions. The electron microprobe results suggest that each CE6 IGB has homogeneous chemical compositions (hereafter referred to as Homo-IGBs; Supplementary Data 2). Most CE6 Homo-IGBs plot in the classification diagram of lunar glasses in the highlands (15) to mare (12) domains, except for WGP09,G31, which plots in the picritic domain in chemistry, suggesting an impact origin (Fig. 2).

The CE6 Homo-IGBs were measured to have equivalent water abundances of ~10–1070 μg.g^{-1} with H isotope compositions (in

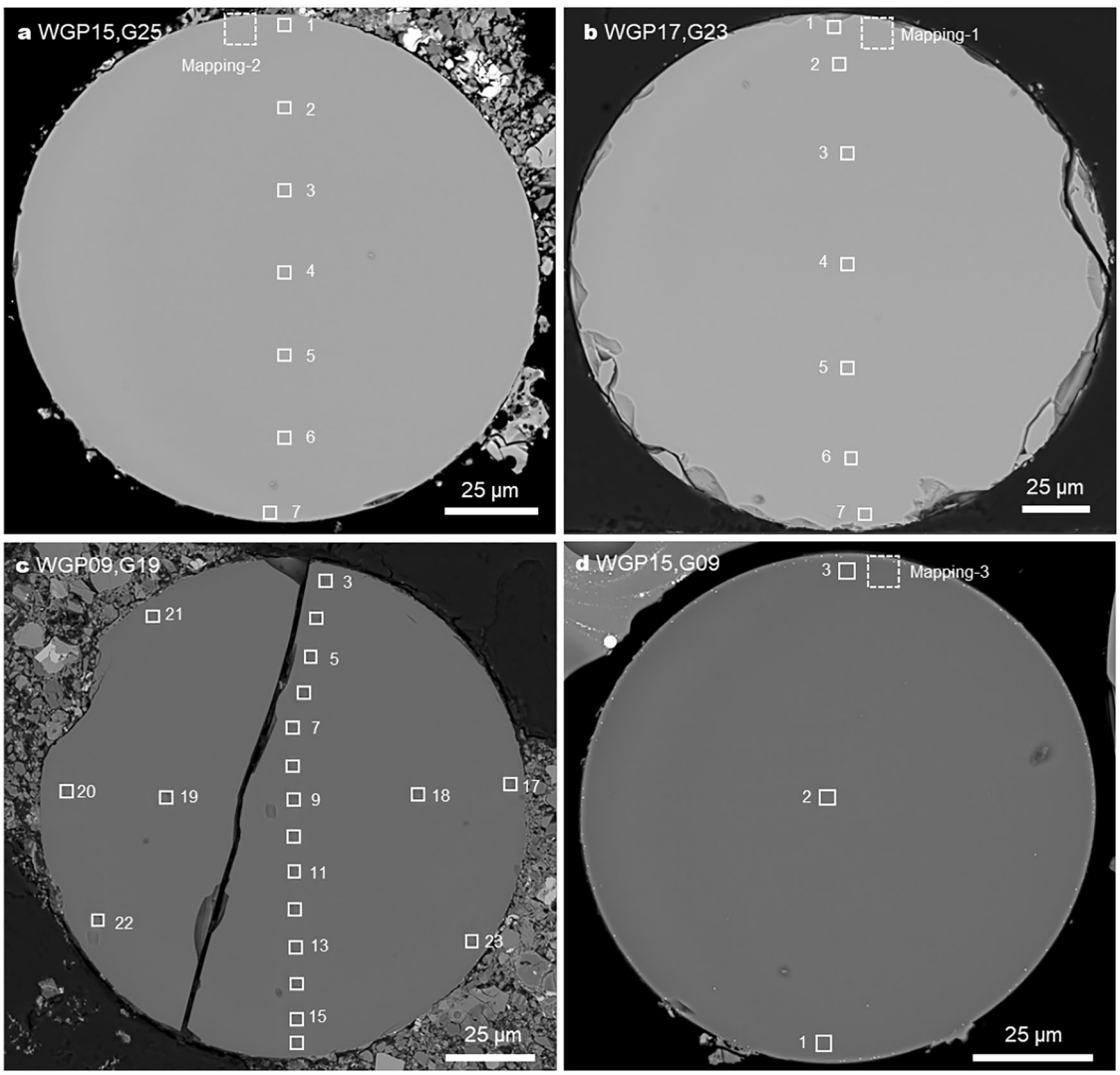

Fig. 1 | Representative petrographic textures of mare and highlands Chang'e-6 (CE6) homogeneous impact glass beads (Homo-IGBs). a WGP15,G25 and (**b**) WGP17,G23 are mare Homo-IGBs. **c** WGP09,G19 and (**d**) WGP15,G09 are two highlands Homo-IGBs. In this study, 28 individual Homo-IGBs were found (Supplementary Figs. 1–3). Among them, one is picritic, 12 are mare, and 15 are highlands (Supplementary Data 2). The white squares with numbers are the NanoSIMS analytical positions. Three NanoSIMS mapping locations are outlined with dashed squares at the margins of the beads.

https://doi.org/10.1038/s41467-025-60388-y

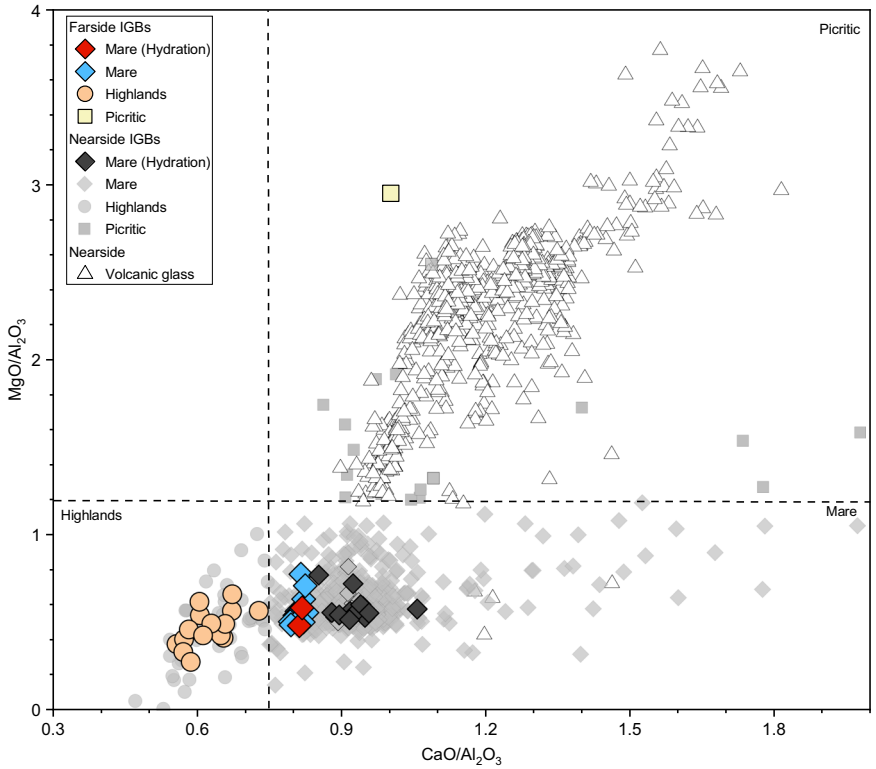

Fig. 2 | MgO/Al_2O_3 versus CaO/Al_2O_3 for the Chang'e-6 (CE6) homogeneous impact glass beads (Homo-IGBs). Most of the CE6 Homo-IGBs are plotted within both highlands and mare domains, except one (WGP09,G31) in the picritic domain. The classification criteria (dash lines) of lunar glasses are referred to refs. 65,66. The datasets of the lunar volcanic glasses and impact glass beads in the nearside are from ref. 48 (Source Data). The observed SW-H_2O hydration profiles are exclusively identified in the mare Homo-IGBs. The source EPMA data of CE6 Homo-IGBs are listed in Supplementary Data 2. The average values of CE6 and CE5 Homo-IGBs are compiled in Source Data. IGBs, impact glass beads.

notation of δD, $\delta D = 1000 \times (D/H_{sample}/D/H_{SMOW}\text{-}1)$, where D/H_{SMOW} is the D/H ratio of the standard mean ocean water; Methods) ranging from − 988 ± 61 to 3718 ± 535‰ after spallation correction at a cosmic ray exposure age of 108 million years ago (Fig. 3 and Supplementary Data 3; Methods). The highlands Homo-IGBs contain ~10–150 μg.g^{-1} H_2O, with δD of − 951‰ to 3718‰. The H_2O content in mare IGBs ranges from ~10 to 1070 μg.g^{-1}, with δD values between − 988‰ and 1778‰. The picritic impact glass bead has 18–161 μg.g^{-1} H_2O and δD values ranging from 32‰ to 2509‰ (Supplementary Data 3). Each CE6 Homo-IGB was carefully measured at the margins to the centres to investigate the potential hydration profiles of SW-H_2O (Supplementary Data 3). Eight profiles were conducted on 7 Homo-IGBs to determine the distribution of water and its isotopic compositions through these targets (Fig. 4 and Supplementary Fig. 4). Two mare Homo-IGBs (WGP15,G25 and WGP17,G23) have hydration profiles showing elevated H_2O (309–1070 μg.g^{-1}) at the outermost margins and sharply decrease to tens of μg.g^{-1} level (Figs. 4a, c). The NanoSIMS mapping results show that the H_2O-enriched layers at the margins of WGP15,G25 and WGP17,G23 are < 4 μm in their widths (Fig. 5 and Supplementary Fig. 5). The other IGBs were not identified to have SW-H_2O hydration profiles like WGP15,G25 and WGP17,G23 (Fig. 4 and Supplementary Figs. 4and 6). Those CE6 Homo-IGBs without hydration profiles have relatively limited intra-bead variations in water abundances (from 34 ± 8 to 102 ± 28 μg.g^{-1}, 1 SD) and δD values (− 348 ± 305 to 2115 ± 606‰, 1 SD) estimated on the profile analyses (Fig. 4, Supplementary Fig. 4 and Data 3). Most CE6 Homo-IGBs contain water abundances <150 μg.g^{-1} (Figs. 3, 6 Supplementary Data 3). All CE6 Homo-IGBs display a notably negative correlation between water abundances and δD values (Fig. 3and Supplementary Data 3). It is interesting to note that the water abundances in the CE6 Homo-IGBs display a dependence on chemical compositions (Figs. 2, 6, 7 and Supplementary Figs. 7, 8). The mare Homo-IGBs have a higher water abundance and a lower δD value than that of highlands and picritic ones (Figs. 6, 7and Supplementary Data 3). Meanwhile, SW-H_2O hydration profiles were only observed in mare Homo-IGBs (Figs. 4, 5 and Supplementary Figs. 4–6).

Universal role of mare IGBs in storage of surface water

The CE6 mare Homo-IGBs collected from the farside exhibit a clear negative correlation in H_2O–δD space, both individual analytical spots and individual IGBs, plotting along the same trend defined by the mare Homo-IGBs collected in the nearside hemisphere (Fig. 3). This negative correlation (Fig. 3) is likely due to a binary endmember mixing rather than the degassing of water under high temperature conditions during the formation of the IGBs[16]. The H_2O-rich spots measured in CE6 mare Homo-IGBs are extremely depleted in deuterium (δD = −988‰; Fig. 3 and Supplementary Data 3). This distinct hydrogen isotopic signature is associated with a solar wind origin[33,34]. These features suggest that SW-H_2O can be globally documented by the mare Homo-IGBs independent of geographic locations. Thus, mare Homo-IGBs, a common component in lunar soils, may have played an important role in the recharge, release, and recycling of water on the Moon[16,31,35].

Such a prediction is further supported by the hydration profiles of CE6 mare Homo-IGBs, which depict the pathways for how the SW-H_2O has been preserved in the IGBs (Fig. 4a–d). Theoretically, the maximum penetration depth of solar wind into the lunar surface minerals is ~ 50–100 nm (refs. 18,36.), which is two orders of magnitude lower than the H_2O-rich and δD-poor bands (~2.2–3.2 μm) observed in CE6 mare Homo-IGBs (Fig. 5and Supplementary Fig. 5). It requires additional post-implantation processes to drive the implanted SW-H_2O moving inwards as well as outwards to form a thicker hydrated layer of SW-H_2O in the IGBs than the theoretical calculations and ground observations[18,36]. There is another possibility that water vapour created

https://doi.org/10.1038/s41467-025-60388-y

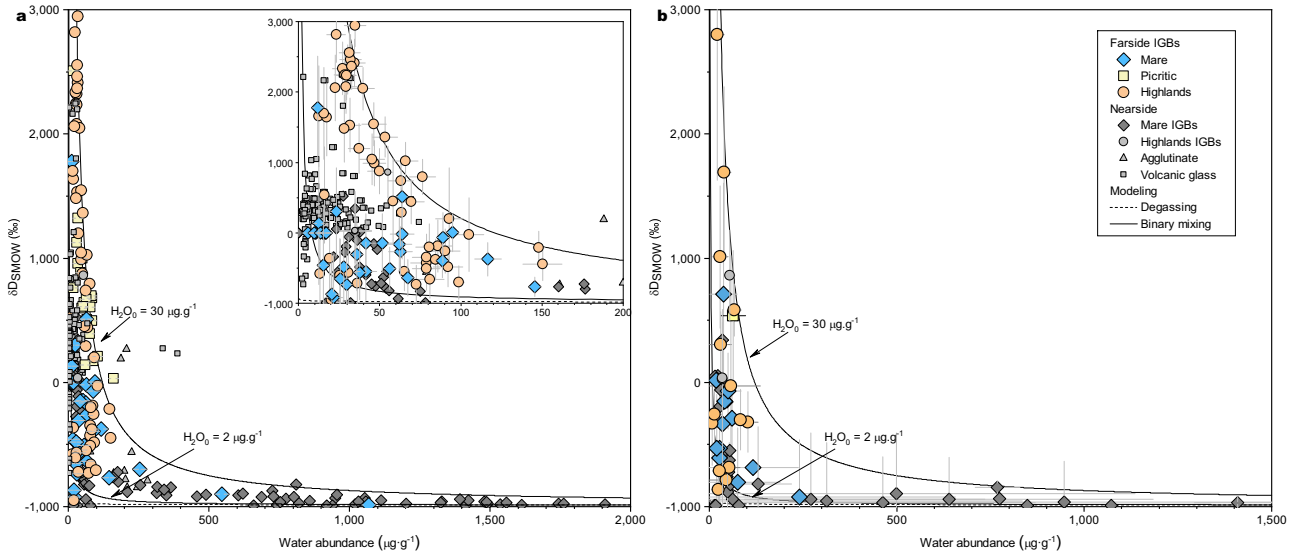

Fig. 3 | Water abundances and δD values of Chang'e-6 (CE6) homogeneous impact glass beads (Homo-IGBs). a The water abundances and hydrogen isotope compositions (δD) of the CE6 Homo-IGBs exhibit a negative correlation, similar to the trend observed in lunar nearside Homo-IGBs. This negative correlation between H_2O and δD can be explained by a binary endmember mixing model[16]. One endmember represents solar wind-derived water, with a concentration of 2000 μg.g^{-1} and a δD value of − 990‰. The other endmember corresponds to the initial water derived from the precursor materials of the impact glass beads, with H_2O of 2–30 μg.g^{-1} and a δD value of ~ 3000‰. The inset is an amplified plot with H_2O from 0 to 200 μg.g^{-1}. The data of CE6 Homo-IGBs are listed in Supplementary Data 3. The error bars are 2σ. **b** The average water abundance and δD of individual Homo-IGBs. The H_2O error bars are 1 SD of the measured values, and the δD errors are 1 SD of the measured D/H ratios. Literature data for nearside glasses in (**a**) include: CE5 mare impact glass[16], volcanic glass beads[68,70], and agglutinates[71], listed in Source Data. Average values of farside and nearside impact glass beads (IGBs) in (**b**) are listed in Source Data.

by asteroid impacts may have driven the ingress of water in the molten silicate droplets which finally quenched to form IGBs. Taken-up of intermediate volatiles (e.g., Na, K, and Cu) from a transit plume[37] during eruption of volcanism on the Moon has been observed in pyroclastic glass beads 74220 (ref. 38). However, the profile analyses of these volcanic glass beads did not exhibit hydration profiles instead of typical degassing profiles of H_2O, as well as other highly volatile elements F, Cl, and S (ref. 3). Moreover, the asteroid impacts on the Moon could result in melting of various components in the target soils/rocks, yielding an average δD value of ~0‰ (ref. 39) for the water in the transit plume. Such a higher δD value (~0‰) of the plume is in conflict with the almost pure solar wind component (δD = −990‰) preserved in the margins of CE6 mare Homo-IGBs. Therefore, the first scenario, post-implantation diffusion processes of solar wind, is deemed more plausible than the ingress model of H_2O from a transit plume to explain the observations from the CE6 mare Homo-IGBs.

Less SW-H_2O stored in lunar farside mare IGBs

The CE6 mare Homo-IGBs, collected from the lunar farside, display contrasting distribution features of water compared with those collected from the Moon's nearside (Figs. 5, 6, 8, Supplementary Fig. 5). One distinct difference is that the widths (< 4 μm) of the SW-H_2O hydration profiles preserved in the farside CE6 mare Homo-IGBs are notably narrower than those observed (up to 40 μm) in the nearside CE5 mare Homo-IGBs (Fig. 5and Supplementary Fig. 5). We carefully investigated the 28 individual CE6 impact glass bead, which may have helped reduce sampling bias (Supplementary Data 3). In comparison, 12 of 33 measured CE5 Homo-IGBs display notable solar wind hydration profiles[16]. Thus, we assume that the datasets measured in the lunar Homo-IGBs from both hemispheres should reflect the intrinsic characteristics.

The narrow widths of the hydration profiles of SW-H_2O found in the CE6 mare Homo-IGBs may be associated with local temperature[23], flux of solar wind on the farside[40], local magnetic anomalies[41–43], and/or their geologic exposure history[44]. In terms of local temperature, the landing sites of CE5 (43.058°N; ref. 45) and CE6 (41.625°S; ref. 46) missions have comparable geographic latitudinal positions, indicating the diurnal temperature variations at both sites should have a comparable range[23], eliminating it as the main reason for the distinct distribution of water in the CE6 mare Homo-IGBs (Figs. 6, 8). Regarding the flux of solar wind protons on the lunar farside, the lunar surface flux is modelled to be higher on the farside than on the nearside[40], indicating the potential for more contributions of SW-H_2O in the lunar farside materials, which is opposite to our observations, thereby also ruling it out as a potential explanation. Regions of magnetic anomalies have been recently discovered on the Moon[43], potentially shielding or reflecting solar wind from implantation into surface materials[41]. However, no magnetic anomaly has been found at the landing site of CE6 (ref. 43). Its exposure history, constrained by the isotopic dating of the return mare basalt fragments of CE6 is ca. 2.8 billion years ago[44], older than that the ca. 2.0 billion-year-old CE5 (ref. 47), indicating that CE6 mare Homo-IGBs may have had more opportunity to receive SW-H_2O during the formation and gardening of lunar soils because of its longer exposure time[32], which again is opposite to our observations, ruling out an exposure age explanation. Therefore, the contrasting hydration profiles depths between the nearside CE5 and farside CE6 remains an enigma worth of further study.

Dichotomic SW-H_2O storage between mare and highlands IGBs

Beyond the differences between them, the CE6 and CE5 Homo-IGBs share a notable similarity in that their SW-H_2O hydration profiles are only identified in the mare Homo-IGBs from both hemispheres (Figs. 4, 5 and Supplementary Figs. 4–6), suggesting that recharge of SW-H_2O in Homo-IGBs is likely composition dependent. CE6 lunar soils contain notably more highlands Homo-IGBs (~54%; Supplementary Data 1) than CE5 soils (~8%; refs. 16,48), providing adequate targets to investigate the storage and release of SW-H_2O in mare and highlands Homo-IGBs. The highlands Homo-IGBs identified in CE6 would have been delivered from non-mare units in the vicinity of the CE6 landing site or quenched from highlands ejecta accompanying with the formation of mare Homo-IGBs. Both scenarios share a co-exposure history in a time span of ca. 2.8 billion years ago (Ga; refs. 44,49), providing equivalent

https://doi.org/10.1038/s41467-025-60388-y

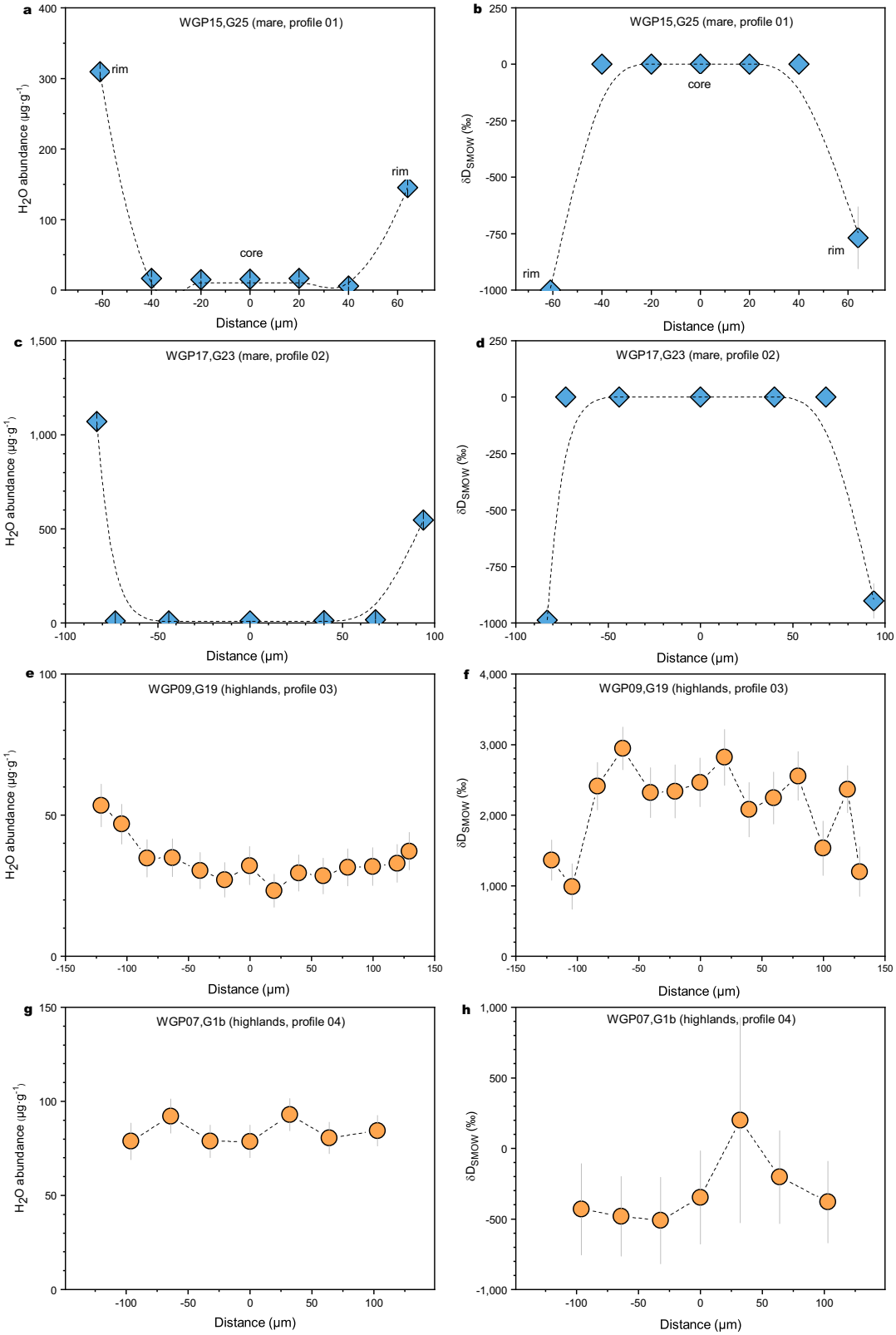

opportunities to receive SW-H_2O and to release of SW-H_2O caused by mild heating events on the near surface of the Moon. Therefore, the CE6 highlands Homo-IGBs would have experienced similar recharge and release of SW-H_2O as the mare ones in the past 2.8 Ga, yielding similar hydration and dehydration profiles of SW-H_2O, contrary to the observations (Fig. 4and Supplementary Fig. 4). In another aspect, provided the CE6 highlands Homo-IGBs had been recharged with SW-H_2O like mare Homo-IGBs but later altered by some heating events, we should expect to observe the hydration and dehydration signatures of SW-H_2O in highlands IGBs. However, most CE6 highlands Homo-IGBs measured have notably higher δD values (500–3000‰; Supplementary Data 3) than that of SW-H_2O (about −990‰; ref. 16). Combining these considerations, the CE6 highlands Homo-IGBs seem to be more resistant to diffusion of SW-H_2O than the mare ones (Figs. 3, 4; ref. 35).

https://doi.org/10.1038/s41467-025-60388-y

Fig. 4 | Typical H_2O and δD profiles measured on Chang'e-6 (CE6) homogeneous impact glass beads (Homo-IGBs). **a**–**d** are profiles measured on two CE6 mare Homo-IGBs (WGP15,G25 and WGP17,G23). **e**–**h** are profiles measured on two CE6 highlands Homo-IGBs (WGP09,G19 and WGP07,G1b). Analytical positions of the outmost rims are measured to be about 3–5 μm to the edges of the impact glass beads (IGBs). All the analytical positions are shown in Fig. 1 and Supplementary Fig. 3. For the mare IGBs, the water abundances in the mantle-centre regions of the IGBs are slightly higher than the instrument H_2O background (**a**, **b**), yielding the large uncertainties on the measured δD. Thus, we treated their δD values as 0‰ for the profile plot. The mare IGBs show SW-H_2O hydration profiles, with H_2O abundance in the rims up to 309 μg.g^{-1} and 1070 μg.g^{-1}, the δD of − 990‰ and − 988‰. The highlands Homo-IGBs do not show SW-H_2O hydration profiles and have relatively limited intra-bead H_2O variations (23–53 μg.g^{-1} and 79–93 μg.g^{-1}, respectively). Meanwhile, these beads have notably higher δD values than that of typical SW-H_2O (about − 990‰) with inter-bead variations of 988 to 2946‰ and − 510 to 200‰, respectively. The error bars are 2σ. The source data are provided in Source Data.

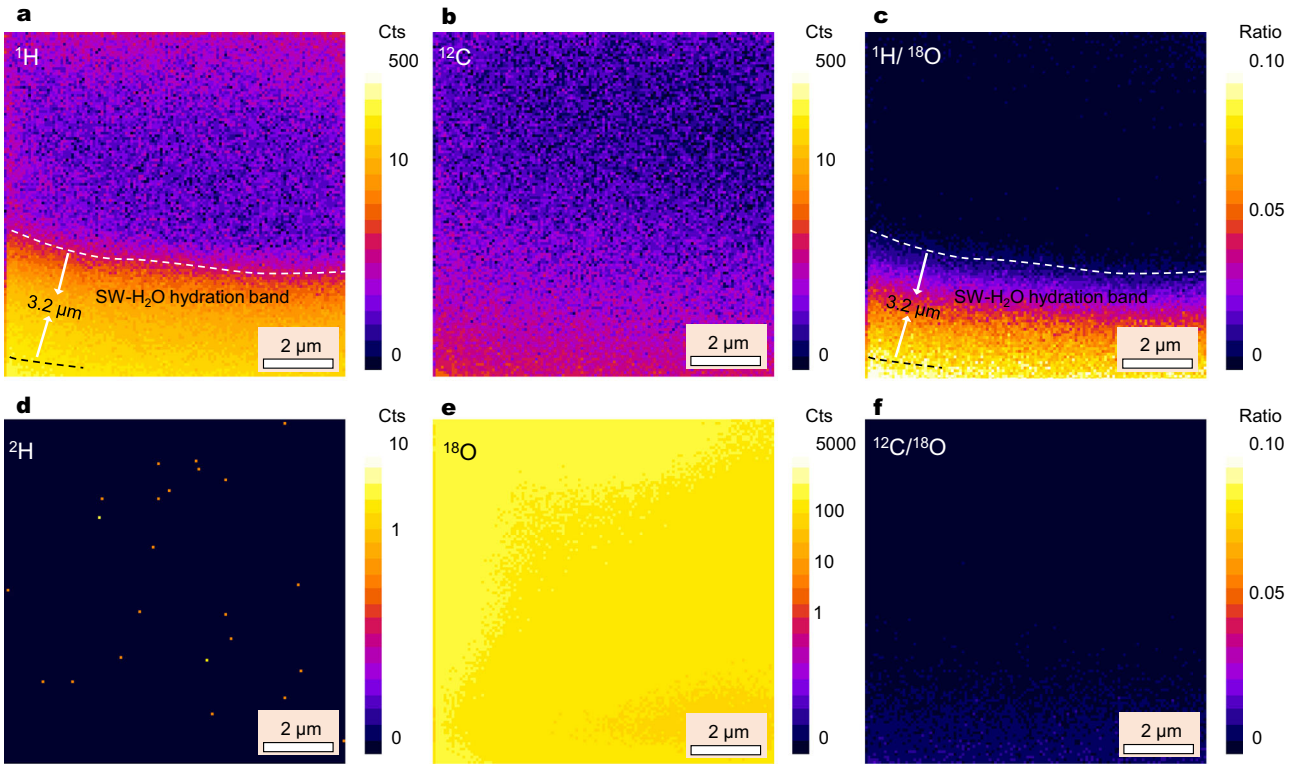

Fig. 5 | NanoSIMS mapping of the distribution of SW-H_2O in WGP17,G23 homogeneous impact glass beads (Homo-IGBs). Distribution of ^{1}H (**a**), ^{2}D (**d**), ^{12}C (**b**), and ^{18}O (**e**) and the derived ^{1}H/^{18}O (**c**) and ^{12}C /^{18}O (**f**) images in the analytical target. The mapping size is 10 μm × 10 μm outlined with a dashed white square in Fig. 1b. The width of the SW-H_2O hydration band on WGP17,G23 is ~ 3.2 μm.

The diffusion of water in matter is mainly relying on the activation energy, diffusion coefficient, and temperature[50]. As discussed above, the local temperatures between the landing sites of CE5 and CE6 are comparable[23]. We therefore infer that the contrast H_2O differences between mare and highlands Homo-IGBs observed in this study (Figs. 3 and 4) are likely composition dependent because the activation energy and diffusion coefficient are relying on chemical compositions[51,52].

To explore the potential relationships between SW-H_2O recharge capacity and Homo-IGBs chemical compositions, we made a comparison between the measured H_2O and chemical compositions (SiO_2, Al_2O_3, TiO_2, and FeO) of Homo-IGBs from both hemispheres (Fig. 7). The H_2O values refer to the maximum value measured in the rims of Homo-IGBs, therefore representing the relative contribution of SW-H_2O. It is clear that the highlands Homo-IGBs host notably lower SW-H_2O than most mare ones (Fig. 7). Meanwhile, SW-H_2O storage of Homo-IGBs exhibits notable dependency on chemical compositions: the Homo-IGBs, with SiO_2 < 43 wt%, Al_2O_3 < 15 wt%, TiO_2 > 3 wt%, and FeO > 17 wt%, hold more SW-H_2O than the rest of the beads (Fig. 7). The regression relationship between chemical composition and SW-H_2O of Homo-IGBs is not linear, indicating that multiple elements may affect the recharge efficiency of SW-H_2O in Homo-IGBs (Fig. 7). Anyhow, the overall trend is obvious and the correlation coefficient (R^2) ranging from ~ 0.6 to 0.8 is strong to very strong (Fig. 7). To further unravel the relationship between SW-H_2O storage and chemical composition in Homo-IGBs, a principal component analysis was carried out. The statistics suggest that FeO and TiO_2 are positively correlated with SW-H_2O, and Al_2O_3, CaO, SiO_2, and MgO are negatively correlated with SW-H_2O, and other elements are insensitive due to their low contents (Supplementary Fig. 8).

The dependence of recharge efficiency of SW-H_2O in Homo-IGBs with chemical compositions carries implications for in situ water utilisation. The highlands Homo-IGBs, characterised by enrichment of Si, Al, and Ca, are more resistant to retain SW-H_2O than mare Homo-IGBs, thus functionally driving release and transportation of SW-H_2O to space and the polar regions[31]. In comparison, the mare Homo-IGBs are capable of storing SW-H_2O in lunar soils, thus functionally buffering the lunar surface water cycle[16]. The lunar surface is characterised by two distinct lithologies, mare basalt and highlands rock[53], the former of which dominantly occurs on the lunar nearside, suggesting that storage of SW-H_2O in Homo-IGBs may exhibit a dichotomy feature coupled with the surface rock types. These features suggest that mare basalt units on the Moon should have higher priorities than the highlands units for in situ water utilisation. Furthermore, within the favourable Homo-IGB mare group, the Fe- and Ti-rich mare

https://doi.org/10.1038/s41467-025-60388-y

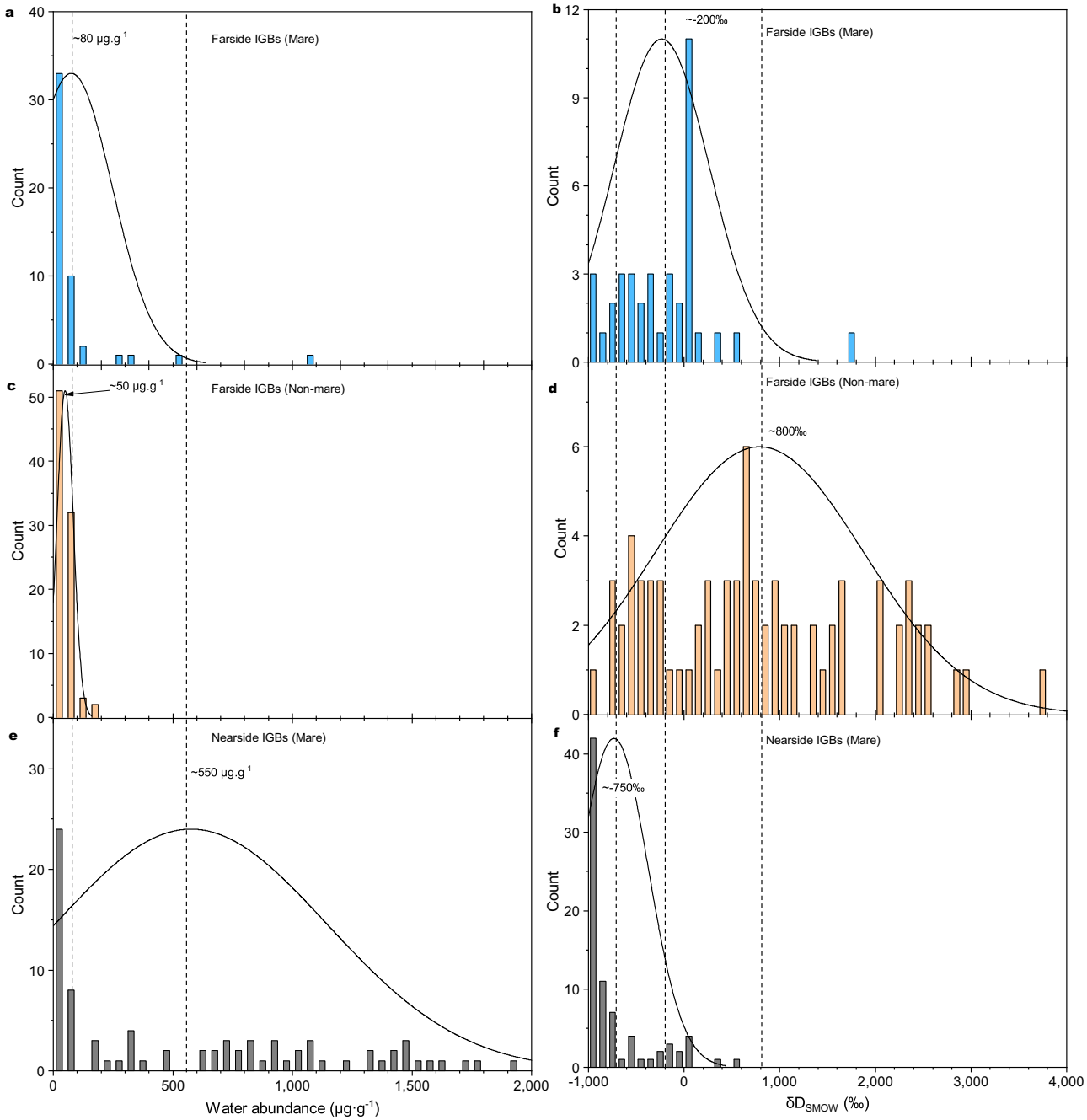

Fig. 6 | Distribution patterns of H_2O and δD of homogeneous impact glass beads (Homo-IGBs) from the farside and nearside of the Moon. a Histogram of H_2O from the farside mare Homo-IGBs. **b** Histogram of δD from the farside mare Homo-IGBs. **c**, **d** are histograms of H_2O and δD from the nearside non-mare (highlands and picritic) Homo-IGBs. **e**, **f** are histograms of H_2O and δD from the nearside mare Homo-IGBs. The farside non-mare Homo-IGBs have an H_2O peak at ~50 μg.g^{-1} lower than that (~80 μg.g^{-1}) of mare Homo-IGBs, and a δD peak at ~800‰ higher than that (about −200‰) of mare Homo-IGBs. In addition, the water abundance of the mare Homo-IGBs from the nearside has another H_2O peak at ~550 μg.g^{-1} with notable SW-H_2O contribution (δD peaked at about − 750‰). Gaussian fit curves are displayed. Nearside datasets are from ref. 16. The source data are provided in Source Data. IGBs, impact glass beads.

units should be prioritised over those Fe- and Ti-poor ones. Therefore, we propose that lunar base construction and water harvesting plants should ideally target lunar nearside Fe- and Ti-rich mare units.

The detailed studies on the Homo-IGBs from both the near and far hemispheres of the Moon suggest that these small beads may have played a big role in storing the solar wind-derived water for the Moon and carry abundant information about the origin, storage, and recycling of mission-critical lunar surface water. These findings provide fundamental information for figuring out the strategies of in situ water utilisation[5]. The recharge of SW-H_2O in Homo-IGBs is thus apparently more complex than previously thought, requiring further studies to shed more light to unravelling the mysteries of these putative targets for sustaining the surface water cycle on the Moon, as well as on other airless bodies[16,30,31,54].

Methods

Sample preparation

Two scooped lunar soil samples CE6C0300YJFM002 (~6 g) and CE6C0200YJFM001 (~5 g) were used in this study. The glass beads, along with some other components, were handpicked under a

https://doi.org/10.1038/s41467-025-60388-y

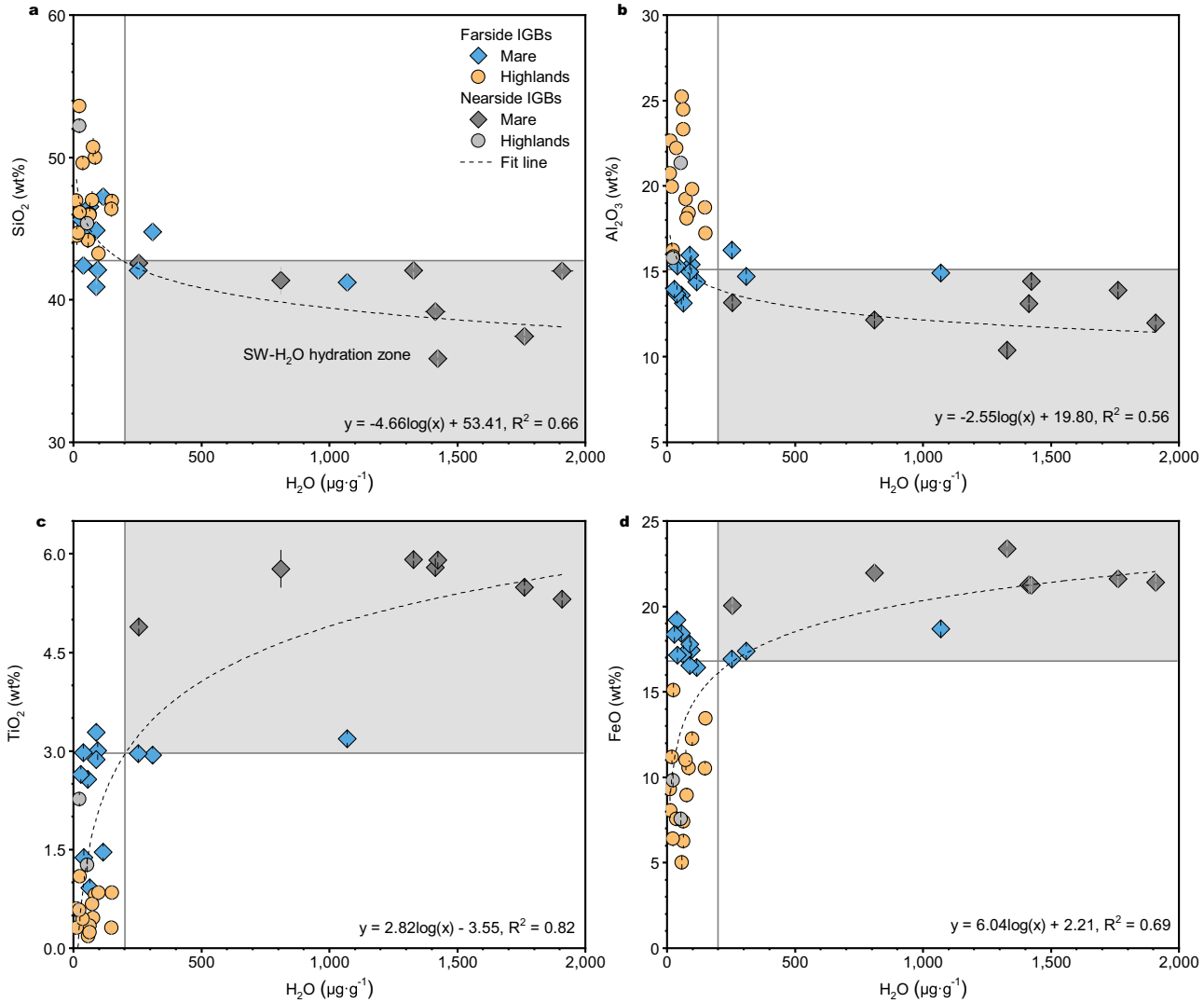

Fig. 7 | Water abundances versus chemical compositions of Chang'e-6 (CE6) homogeneous impact glass beads (Homo-IGBs). The relationship between H_2O abundances with SiO_2 (**a**), Al_2O_3 (**b**), TiO_2 (**c**), and FeO (**d**) of CE6 Homo-IGBs. The chemical compositions are the average values measured by electron probe microanalyser for individual impact glass beads (IGBs). Water abundances are referred to the values measured at the edges of the individual IGBs, thus representing the apparent contributions of SW-H_2O. The highlands Homo-IGBs host remarkable less water than mare ones. Meanwhile, water abundances in Homo-IGBs exhibit a logarithmic positive correlation with TiO_2 and FeO and a logarithmic negative correlation with SiO_2 and Al_2O_3. The light grey rectangles are the regions with notable SW-H_2O hydration profiles. The source data are provided in Source Data.

binocular microscope in the ultraclean room at the Institute of Geology and Geophysics, Chinese Academy of Sciences (IGGCAS) in Beijing. The sample preparation methods can be referred to He et al. [55]. The picked particles were placed in a tunnel of silica glass cut by low-speed diamond saw and then mounted by epoxy and prepared into polished thick sections labelled as WGP01 to WGP18 (Supplementary Fig. 1). The glass beads in the sample mounts, WGP07, 09, 10, 15, and 17 were extensively measured in this work (Supplementary Data 1). The prepared sections were cleaned up using anhydrous ethanol prior to drying at 50 °C in a baking oven. All the mounts were coated with carbon for petrographic observation and chemical analysis. The coating was replaced with Au for water abundance and hydrogen isotopic analysis.

Scanning electron microscopy

Petrographic observations were carried out using field emission scanning electron microscopy (FE-SEM) on a FEI Nova NanoSEM 450 at IGGCAS, using electron beam currents of 6.4 nA and an acceleration voltage of 15 kV. The prepared sections were initially coated with carbon for petrographic observations, and then recoated with Au for in situ NanoSIMS measurement of water content and hydrogen isotopes. After NanoSIMS analyses, the original coating was removed, and the samples were cleaned and recoated with carbon for SEM observation to confirm the positions of the NanoSIMS spots (Supplementary Fig. 3).

Electron probe microanalysis

The major elements abundances of the impact glass beads were measured using a JEOL JXA-8100 electron probe micro-analyser (EPMA) at IGGCAS. The accelerating voltage was 15 kV and the beam current was 10 nA, with a beam size of 10 μm in diameter. The standards were albite for Na and Al, diopside for Si, Mg, and Ca, magnetite for Fe, bustamite for Mn, sanidine for K, rutile for Ti, Cr_2O_3 for Cr, NiO for Ni, and a natural obsidian glass was used as a monitor. The detection limits were 0.02 wt.% for MgO and NiO, < 0.01 wt.% for Na_2O, Cr_2O_3, Al_2O_3, MnO, K_2O, SiO_2, FeO, CaO, and TiO_2. The analytical results are listed in Supplementary Data 2.

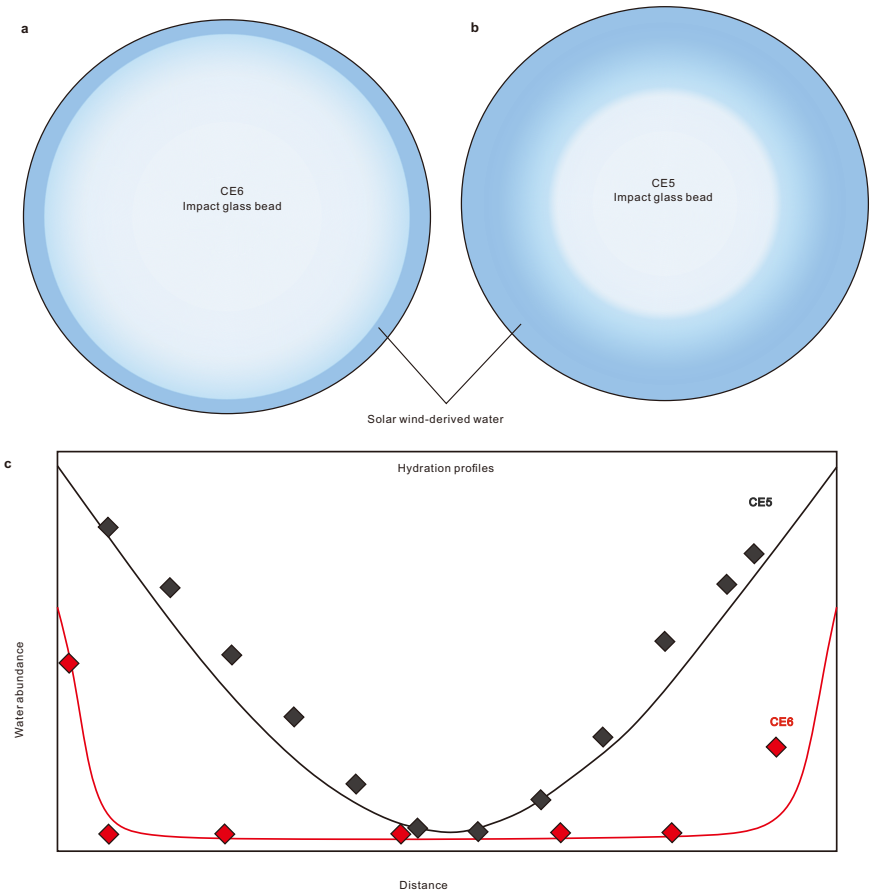

Fig. 8 | Comparison of the distribution of SW-H_2O in farside and nearside homogeneous impact glass beads (Homo-IGBs). a, **b** The hydration layer of SW-H_2O in farside Homo-IGBs with an observed maximum depth < 4 μm (CE6, this study; Figs. 4 and 5) compared to the distribution of SW-H_2O in the nearside Homo-IGBs (CE5; ref. 16). **c** Comparison of the deepest hydration profiles measured in the nearside (CE5; ref. 16) and the farside impact glass beads (IGBs) (CE6; Figs. 4 and 5, Supplementary Fig. 5). The source data for the plots are provided in Source Data. CE5, Chang'e-5; CE6, Chang'e-6.

In situ water abundance and hydrogen isotope composition analysis

In situ water abundance and hydrogen isotope analysis were conducted using a CAMECA NanoSIMS 50 L at IGGCAS, following a well-used analytical protocol described in Hu et al.[56] and Barnes et al.[57]. The prepared samples and standards were placed in the same holder and stored in the airlock of the NanoSIMS 50 L. They were baked at ~60 °C in the airlock more than 12 h to reduce the hydrogen background during analysis. Then, the sampled were stored in the vessel chamber under high vacuum conditions prior to measurements of water abundances and hydrogen isotopic compositions. The vacuum pressure in the analysis chamber was ~ 2.0×10^{-10} mbar during analysis, facilitated by a liquid nitrogen trap[58]. Each 10 μm × 10 μm analysis area was pre-sputtered for 2 min with a Cs^+ ion beam current of 5 nA to remove the surface coating and potential contamination. A 5 μm × 5 μm region of interest on targets was selected for analysis. Secondary anions $^1H^-$, $^2D^-$ $^{12}C^-$, and $^{18}O^-$ were simultaneously counted by electron multipliers for 400 cycles from the central 50% area (3 μm × 3 μm) using the electronic gate technique of NanoSIMS. The acquisition time is ~4 min for each measurement. The primary beam current (Fco) was ~0.5 nA for analysis with a beam size of ~500 nm in diameter. The charging effect on the samples surface was compensated by an electron-gun during analysis. The real time images (RTI) of $^1H^-$ and $^{12}C^-$ were used to monitor the analytical locations and potential contaminations.

The calibration line for water abundance was established using a series of glass and apatite standards, including SWIFT MORB glass (H_2O = 2580 μg.g^{-1}), Kovdor apatite (H_2O = 9800 ± 700 μg.g^{-1})[59], Durango apatite (H_2O = 480 μg.g^{-1})[60,61], and two basaltic glasses, ALV-519-4-1 (H_2O = 1,700 μg.g^{-1})[62] and ALV-1833-11 (H_2O = 12,000 μg.g^{-1})[62] (Supplementary Data 4;and Fig. 9). Instrument mass fractionation (IMF) on hydrogen isotope composition was corrected using the SWIFT MORB glass (δD = − 73 ± 2‰), and monitored by Kovdor apatite (δD = −66 ± 21‰)[59] and Durango apatite (δD = − 120 ± 5‰)[60,61], as the matrix effect on hydrogen isotope composition are same between silicate glass and apatite within analytical uncertainties[56]. The basaltic glasses ALV-519-4-1 and ALV-1833-11 were also used to monitor the stability of instrumental mass fractionation of hydrogen isotopes throughout the analytical session, yielding comparable δD values to previous values[2] within analytical uncertainties (Supplementary Data 4and Fig. 10). Hydrogen isotopic compositions are given using the delta notation, $\delta D = ((D/H)_{sample}/(D/H)_{SMOW}) - 1) \times 1000$ ‰, where SMOW is the standard mean ocean water with a D/H ratio of 1.5576×10^{-4}.

The instrument H background was detected by a San Carlos olivine[63] (H_2O ~ 1.4 μg.g^{-1}) and a synthetic anhydrous silica glass Suprasil 3001. The H background correction was referred to ref. 64., following the relationship: $H/O_{bg} = (H_{counts} - H_{bg}) / O_{counts}$ and $D/H_{measured} = (1\text{-}f) \times D/H_{true} + f \times D/H_{bg}$, where f is the proportion of H emitted from the instrumental background. The instrument background has gradually decreased as the sample stored in the instrument for longer time. In the first four days of the analysis session, a slightly higher instrument background at 15 ± 5 μg.g^{-1} (D/H_{bg} average was (1.49 ± 0.75) × 10^{-4} and H_{bg} was 516 ± 164 counts per second (cps)). For

the following four days, the instrument H_2O background was 7 ± 1 μg.g^{-1} (D/H_{bg} average was $(2.71 \pm 1.67) \times 10^{-4}$ and H_{bg} was 259 ± 50 cps) (Supplementary Data 4). After background subtraction, the water abundances of the IGBs were quantitatively calculated based on the H_2O content calibration line established on the standards (Supplementary Data 3).

For notable hydration profiles, we also used a low Fco (~ 100 pA) to carry out high spatial resolution mapping analyses for acquiring the distribution of SW-H_2O from the edge to the inner side of the IGBs after the spot measurements. The mapping results suggest that the SW-H_2O hydration depths are ~ 2.2 μm for WGP15,G25 (Supplementary Fig. 5) and ~ 3.2 μm for WGP17,G23 (Fig. 5). But the SW-H_2O hydration band was not observed on WGP15,G09 (Supplementary Fig. 6).

Petrography of CE6 IGBs

A total of 263 particles were mounted in five sample mounts (WGP07, 09, 10, 15, and 17). Seventy-seven impact glass beads (IGBs) were identified among these particles (Supplementary Data 1). These IGBs exhibit various textures (Supplementary Fig. 1). Twenty-eight of them have smooth exposed surface without any inclusions or vesicles (Fig. 1 and Supplementary Fig. 3), hereafter referred as Homo-IGBs. The other IGBs are characterised by the presence of vesicles, bubbles, mineral clasts, sulfide droplets, and spherical Fe-Ni metals (Supplementary Fig. 2). The Homo-IGBs were selected to investigate the potential SW-H_2O hydration process in the farside IGBs and to find out the common processes may have happened in both nearside and farside IGBs. CE6 Homo-IGBs exhibit round to elliptical shapes with diameters ranging from ~50 μm to ~300 μm (Supplementary Fig. 3). Two of the Homo-IGBs are coated by some finer dusts (Supplementary Fig. 3). These Homo-IGBs display inter-bead contrasts, indicative of varied chemical compositions (Fig. 1and Supplementary Fig. 3).

Chemistry

The chemical composition of CE6 Homo-IGBs were carefully measured using EPMA (Supplementary Data 2). Each Homo-IGB has relatively homogeneous chemical compositions compared with the large inter-bead variations (Supplementary Data 2), consistent with the contrast difference observed using SEM (Fig. 1 and Supplementary Fig. 3). The studied CE6 Homo-IGBs are plotted in three domains on the classification diagram of lunar glasses[65,66], highlands (15), mare (12), and picritic (1) (Fig. 2 and Supplementary Data 2). CE6 Homo-IGBs have notably more highlands beads than CE5 Homo-IGBs[16,48], consistent with the characterisation of the CE6 soil samples[46]. The CE6 picritic glass (WGP09,G31) contains notably lower Al_2O_3 (6.3–6.9 wt%) and CaO (6.4–6.9 wt%) and higher MgO (18.7–20.2 wt%) than highlands and mare Homo-IGBs (Supplementary Data 2, Fig. 7). The CE6 highlands Homo-IGBs contain lower TiO_2 (0.6 ± 0.6 wt%) and FeO (9.7 ± 5.4 wt%) and higher Al_2O_3 (19.9 ± 5.4 wt%) (Supplementary Data 2 and Fig. 7). The CE6 mare Homo-IGBs have comparable chemical compositions with CE5 mare Homo-IGBs except slightly lower TiO_2 (0.82–3.38 wt%) and FeO (16.0–19.8 wt%) and higher SiO_2 (40.4–47.6 wt%) (Supplementary Data 2and Fig. 7). All Homo-IGBs contain minor Cr_2O_3, Na_2O, and MnO (Supplementary Data 2). It is observed that the highlands and picritic Homo-IGBs are plotted along the same trend in the diagram of CaO versus Al_2O_3, exhibiting a lower slope than the mare Homo-IGBs (Supplementary Fig. 7f). Three highlands Homo-GBs (WGP09,G19, WGP15,G06 and WGP17,G02) were observed to have sodium oxide profiles decrease from the rims towards the centres (Supplementary Fig. 11).

Correction of water abundances and D/H ratio for spallation effect

The measured D/H ratios have been corrected for cosmic-ray spallation effect, using a deuterium production rate of 2.17×10^{-12} mol.g^{-1}.Myr^{-1} (Myr, million years; ref. 67). The correction introduces error of comes from the 50% uncertainty of the H and D produce rate (Supplementary Data 3; ref. 68). A cosmic ray exposure age of 108 Myr used for CE6 (ref. 55) was applied in this study to ensure the maximum correction for the extremely elevated D/H ratios.

Degassing modelling

The change in the hydrogen isotopic composition during volatile degassing into a vacuum can be modelled using Rayleigh distillation, expressed as:

$$\delta_{final} = \delta_{initial} + (1,000 + \delta_{initial}) \times (F^{(\alpha-1)} - 1) \quad (1)$$

where $\delta_{initial}$ and δ_{final} are the initial and instantaneous isotopic compositions of the material formed IGBs, F is the fraction of the element remaining, and α is the fractionation coefficient. The fractionation coefficient α is determined by the volatile species losing into a vacuum, governed by Graham's law and given by $\alpha^2 = M_2/M_1$, where M_1 is the molar mass of the heavy isotopologue, and M_2 is the molar mass of the volatilising light isotopologue. For the degassing trend shown in Fig. 2, we assume that the IGBs have an the initial water abundance of 2000 μg.g^{-1}, with a δD value of −990‰ based on the measured datasets (Supplementary Data 3), and degas in the form of H_2 ($M_1 = 2$ for H_2 and $M_2 = 3$ for HD), yielding an α value of ~ 0.8165 (ref. 69).

Data availability

All geochemical data generated in this study are included in Supplementary Data 1–4. The data used in the figures and Supplementary Figures are combined as Source Data. All the datasets are available on Figshare at https://doi.org/10.6084/m9.figshare.28648742. Source data are provided in this paper.

Code availability

No code is used in this study.

References

1. Raymond, S. N., Quinn, T. & Lunine, J. I. Making other earths: dynamical simulations of terrestrial planet formation and water delivery. *Icarus* **168**, 1–17 (2004).
2. Hu, S. et al. A dry lunar mantle reservoir for young mare basalts of Chang'e-5. *Nature* **600**, 49–53 (2021).
3. Saal, A. E. et al. Volatile content of lunar volcanic glasses and the presence of water in the Moon's interior. *Nature* **454**, 192–195 (2008).
4. Peslier, A. H. & De Sanctis, M. C. Water in differentiated planets, the Moon, and asteroids. *Elements* **18**, 167–173 (2022).
5. Crawford, I. A. et al. Lunar resources. *Rev. Mineral. Geochem.* **89**, 829–868 (2023).
6. Hurley, D. M. et al. Surface volatiles on the Moon. *Rev. Mineral. Geochem.* **89**, 787–827 (2023).
7. Clark, R. N. Detection of adsorbed water and hydroxyl on the Moon. *Science* **326**, 562–564 (2009).
8. Colaprete, A. et al. Detection of water in the LCROSS ejecta plume. *Science* **330**, 463–468 (2010).
9. Honniball, C. I. et al. Molecular water detected on the sunlit Moon by SOFIA. *Nat. Astron.* **5**, 121–127 (2020).
10. Feldman, W. C. et al. Fluxes of fast and epithermal neutrons from Lunar Prospector: evidence for water ice at the lunar poles. *Science* **281**, 1496–1500 (1998).
11. Li, S. et al. Widespread hematite at high latitudes of the Moon. *Sci. Adv.* **6**, eaba1940 (2020).
12. Li, S. et al. Direct evidence of surface exposed water ice in the lunar polar regions. *Proc. Natl. Acad. Sci. USA* **115**, 8907–8912 (2018).
13. Bandfield, J. L., Poston, M. J., Klima, R. L. & Edwards, C. S. Widespread distribution of OH/H(2)O on the lunar surface inferred from spectral data. *Nat. Geosci.* **11**, 173–177 (2018).

14. Milliken, R. E. & Li, S. Remote detection of widespread indigenous water in lunar pyroclastic deposits. *Nat. Geosci.* **10**, 561–565 (2017).
15. Mitrofanov, I. G. et al. Hydrogen mapping of the lunar south pole using the LRO neutron detector experiment LEND. *Science* **330**, 483–486 (2010).
16. He, H. C. et al. A solar wind-derived water reservoir on the Moon hosted by impact glass beads. *Nat. Geosci.* **16**, 294–300 (2023).
17. Zhou, C. et al. Multiple sources of water preserved in impact glasses from Chang'e-5 lunar soil. *Sci. Adv.* **10**, eadl2413 (2024).
18. Zhou, C. et al. Chang'E-5 samples reveal high water content in lunar minerals. *Nat. Commun.* **13**, 5336 (2022).
19. Wang, C. et al. Scientific objectives and payload configuration of the Chang'E-7 mission. *Natl. Sci. Rev.* **11**, nwad329 (2023).
20. Pieters, C. M. et al. Character and spatial distribution of OH/H_2O on the surface of the Moon seen by M3 on Chandrayaan-1. *Science* **326**, 568–572 (2009).
21. Johnson, F. S. Lunar atmosphere. *Rev. Geophys.* **9**, 813–823 (1971).
22. Lucey, P. et al. Understanding the lunar surface and space-Moon interactions. *Rev. Mineral. Geochem.* **60**, 83–219 (2006).
23. Li, S. & Milliken, R. E. An empirical thermal correction model for Moon Mineralogy Mapper data constrained by laboratory spectra and Diviner temperatures. *J. Geophys. Res. Planet.* **121**, 2081–2107 (2016).
24. Robbins, S. J. A new global database of lunar impact craters >1–2 km: 1. crater locations and sizes, comparisons with published databases, and global analysis. *J. Geophys. Res. Planet.* **124**, 871–892 (2019).
25. Lawrence, D. J. et al. Evidence for water ice near Mercury's north pole from MESSENGER Neutron Spectrometer measurements. *Science* **339**, 292–296 (2013).
26. Prettyman, T. H. et al. Elemental mapping by Dawn reveals exogenic H in Vesta's regolith. *Science* **338**, 242–246 (2012).
27. Li, S. & Milliken, R. E. Water on the surface of the Moon as seen by the Moon Mineralogy Mapper: Distribution, abundance, and origins. *Sci. Adv.* **3**, e1701471 (2017).
28. Sunshine, J. M. et al. Temporal and spatial variability of lunar hydration as observed by the Deep Impact spacecraft. *Science* **326**, 565–568 (2009).
29. Wohler, C., Grumpe, A., Berezhnoy, A. A. & Shevchenko, V. V. Time-of-day-dependent global distribution of lunar surficial water/hydroxyl. *Sci. Adv.* **3**, e1701286 (2017).
30. Benna, M., Hurley, D. M., Stubbs, T. J., Mahaffy, P. R. & Elphic, R. C. Lunar soil hydration constrained by exospheric water liberated by meteoroid impacts. *Nat. Geosci.* **12**, 333–338 (2019).
31. Jones, B. M., Aleksandrov, A., Hibbitts, K., Dyar, M. D. & Orlando, T. M. Solar wind-induced water cycle on the moon. *Geophys. Res. Lett.* **45**, 10959–10967 (2018).
32. McKay, D. S. et al. *The Lunar Regolith in Lunar Sourcebook* 285–356 (Cambridge University Press, 1991).
33. Alexander, C. M. et al. The provenances of asteroids, and their contributions to the volatile inventories of the terrestrial planets. *Science* **337**, 721–723 (2012).
34. Robert, F., Gautier, D. & Dubrulle, B. The solar system D/H ratio: Observations and theories. *Space Sci. Rev.* **92**, 201–224 (2000).
35. Farrell, W. M., Hurley, D. M. & Zimmerman, M. I. Solar wind implantation into lunar regolith: Hydrogen retention in a surface with defects. *Icarus* **255**, 116–126 (2015).
36. Xu, Y. et al. High abundance of solar wind-derived water in lunar soils from the middle latitude. *Proc. Natl. Acad. Sci. USA* **119**, e2214395119 (2022).
37. Farrell, W. M. et al. A lingering local exosphere created by a gas plume of a lunar lander. *Icarus* **376**, 114857 (2022).
38. Su, X., Zhang, Y., Liu, Y. & Holder, R. M. Outgassing and in-gassing of Na, K and Cu in lunar 74220 orange glass beads. *Earth Planet. Sci. Lett.* **602**, 117924 (2023).
39. Epstein, S. & Taylor, H. P. Jr. $^{18}O/^{16}O$, $^{30}Si/^{28}Si$, D/H, and $^{13}C/^{12}C$ Studies of Lunar rocks and minerals. *Science* **167**, 533–535 (1970).
40. Kallio, E., Dyadechkin, S., Wurz, P. & Khodachenko, M. Space weathering on the Moon: Farside-nearside solar wind precipitation asymmetry. *Planet. Space Sci.* **166**, 9–22 (2019).
41. Glotch, T. D. et al. Formation of lunar swirls by magnetic field standoff of the solar wind. *Nat. Commun.* **6**, 6189 (2015).
42. Li, S. & Garrick-Bethell, I. Surface water at Lunar magnetic anomalies. *Geophys. Res. Lett.* **46**, 14318–14327 (2019).
43. Vorburger, A. et al. Energetic neutral atom observations of magnetic anomalies on the lunar surface. *J. Geophys. Res. Planet.* **117**, A07208 (2012).
44. Zhang, Q. W. L. et al. Lunar farside volcanism 2.8 billion years ago from Chang'e-6 basalts. *Nature* https://doi.org/10.1038/s41586-024-08382-0 (2024).
45. Li, C. et al. Characteristics of the lunar samples returned by the Chang'E-5 mission. *Natl. Sci. Rev.* **9**, nwab188 (2022).
46. Li, C. et al. Nature of the lunar far-side samples returned by the Chang'E-6 mission. *Natl. Sci. Rev.* **11**, nwae328 (2024).
47. Li, Q. L. et al. Two-billion-year-old volcanism on the Moon from Chang'e-5 basalts. *Nature* **600**, 54–58 (2021).
48. Wang, B.-W. et al. Returned samples indicate volcanism on the Moon 120 million years ago. *Science* **385**, 1077–1080 (2024).
49. Cui, Z. et al. A sample of the Moon's far side retrieved by Chang'e-6 contains 2.83-billion-year-old basalt. *Science* **386**, 1395–1399 (2024).
50. Starukhina, L. Water detection on atmosphereless celestial bodies: Alternative explanations of the observations. *J. Geophys. Res. Planet* **106**, 14701–14710 (2001).
51. Zouine, A., Dersch, O., Walter, G. & Rauch, F. Diffusivity and solubility of water in silica glass in the temperature range 23-200 degrees C. *Phys. Chem. Glasses***48**, 85–91 (2007).
52. Zhang, Y. & Ni, H. Diffusion of H, C, and O components in silicate melts. *Rev. Mineral. Geochem.* **72**, 171–225 (2010).
53. Jolliff, B. L., Gillis, J. J., Haskin, L. A., Korotev, R. L. & Wieczorek, M. A. Major lunar crustal terranes: Surface expressions and crust-mantle origins. *J. Geophys. Res. Planet.* **105**, 4197–4216 (2000).
54. Jones, B. M., Sarantos, M. & Orlando, T. M. A new in situ quasi-continuous solar-wind source of molecular water on mercury. *Astrophys. J. Lett.* **891**, L43 (2020).
55. He, H. et al. Water abundance in the lunar farside mantle. *Nature* https://doi.org/10.1038/s41586-025-08870-x (2025).
56. Hu, S. et al. Measurements of water content and D/H ratio in apatite and silicate glasses using a NanoSIMS 50 L. *J. Anal. At. Spectrom.* **30**, 967–978 (2015).
57. Barnes, J. J. et al. Accurate and precise measurements of the D/H ratio and hydroxyl content in lunar apatites using NanoSIMS. *Chem. Geol.* **337**, 48–55 (2013).
58. Li, R. Y. et al. High-spatial-resolution measurement of water content in olivine using nanoSIMS 50 L. *At. Spectrosc.* **43**, 77–83 (2022).
59. Nadeau, S. L., Epstein, S. & Stolper, E. Hydrogen and carbon abundances and isotopic ratios in apatite from alkaline intrusive complexes, with a focus on carbonatites. *Geochim. Cosmochim. Acta* **63**, 1837–1851 (1999).
60. Greenwood, J. P., Itoh, S., Sakamoto, N., Vicenzi, E. P. & Yurimoto, H. Hydrogen isotope evidence for loss of water from Mars through time. *Geophys. Res. Lett.* **35**, L05203 (2008).
61. Greenwood, J. P. et al. Hydrogen isotope ratios in lunar rocks indicate delivery of cometary water to the Moon. *Nat. Geosci.* **4**, 79–82 (2011).
62. Hauri, E. et al. SIMS analysis of volatiles in silicate glasses. *Chem. Geol.* **183**, 99–114 (2002).
63. Zhang, W. F. et al. Optimization of SIMS analytical parameters for water content measurement of olivine. *Surf. Interf. Anal.* **52**, 224–233 (2019).

64. Tartese, R., Anand, M. & Franchi, I. A. H and Cl isotope characteristics of indigenous and late hydrothermal fluids on the differentiated asteroidal parent body of Grave Nunataks 06128. *Geochim. Cosmochim. Acta* **266**, 529–543 (2019).
65. Delano, J. W. Pristine Lunar glasses: Criteria, data, and implications. *Lunar Planet. Sci. Confer. Proceed.* **91**, D201–D213 (1986).
66. Naney, M., Crowl, D. & Papike, J. The Apollo 16 drill core: Statistical analysis of glass chemistry and the characterization of a High Alumina-Silica Poor (HASP) glass. *Proc. Lunar Sci. Conf.* **7**, 155–184 (1976).
67. Füri, E., Deloule, E. & Trappitsch, R. The production rate of cosmogenic deuterium at the Moon's surface. *Earth Planet. Sci. Lett.* **474**, 76–82 (2017).
68. Saal, A. E., Hauri, E. H., Van Orman, J. A. & Rutherford, M. J. Hydrogen isotopes in lunar volcanic glasses and melt inclusions reveal a carbonaceous chondrite heritage. *Science* **340**, 1317–1320 (2013).
69. Sharp, Z. D., McCubbin, F. M. & Shearer, C. K. A hydrogen-based oxidation mechanism relevant to planetary formation. *Earth Planet. Sci. Lett.* **380**, 88–97 (2013).
70. Füri, E., Deloule, E., Gurenko, A. & Marty, B. New evidence for chondritic lunar water from combined D/H and noble gas analyses of single Apollo 17 volcanic glasses. *Icarus* **229**, 109–120 (2014).
71. Liu, Y. et al. Direct measurement of hydroxyl in the lunar regolith and the origin of lunar surface water. *Nat. Geosci.* **5**, 779–782 (2012).

Acknowledgements

We thank David Chew for providing Durango and Kovdor apatite, Erik Hauri for providing basaltic glass 519-4-1 and 1833-11 and anhydrous Suprasil 3001, Robert Francis for providing SWIFT MORB glass, Yi Chen and Lihui Jia for assistance with EPMA measurement, Hongxia Ma for hand-picking the glass beads, and Lixin Gu and Xu Tang for assistance with SEM observation. This study was funded by the National Natural Science Foundation of China (42241104 to S. H.), China National Postdoctoral Programme for Innovative Talents (BX20240365 to H.-C.H.), and the key research programme of the Institute of Geology and Geophysics, Chinese Academy of Sciences (IGGCAS-202401 and 202204 to S.H.). The CE6 samples were allocated by the China National Space Administration (CNSA).

Author contributions

S.H. designed this research. H.-C.H., L.G., Y.G., M.Q., L.L., Z.Z., R.L., Y.C., L.J., Q.L., W.Y., S.C. and S.H. prepared the sample and characterised the petrography and mineral chemistry of the samples. H.-C.H., Y.G., M.Q. L.L., R.L., J.H. and S.H. conducted the NanoSIMS measurements. S.H., H.-C.H., K.L. and R.M. wrote the manuscript. H.H., Y.L., X.L. and F.W. for discussion. All authors contributed to the preparation of the manuscript.

Competing interests

The authors declare no competing interests.

Additional information

Supplementary information The online version contains supplementary material available at https://doi.org/10.1038/s41467-025-60388-y.

Correspondence and requests for materials should be addressed to Sen Hu.

Peer review information *Nature Communications* thanks the anonymous reviewers for their contribution to the peer review of this work. A peer review file is available.